Journal of Power Sources 196 (2011) 196–207

Contents lists available at ScienceDirect

Journal of Power Sources

journal homepage: www.elsevier.com/locate/jpowsour

Modeling and control of tubular solid-oxide fuel cell systems. I: Physical models and linear model reduction

Andrew M. Colclasure, Borhan M. Sanandaji, Tyrone L. Vincent, Robert J. Kee*

Engineering Division, Colorado School of Mines, 1600 Illinois St., Golden, CO 80401, USA

ARTICLE INFO

Article history:
Received 12 May 2010
Received in revised form 22 June 2010
Accepted 22 June 2010
Available online 30 June 2010

Keywords:
Tubular SOFC
Physical model
System identification
Model reduction

ABSTRACT

This paper describes the development of a transient model of an anode-supported, tubular solid-oxide fuel cell (SOFC). Physically based conservation equations predict the coupled effects of fuel channel flow, porous-media transport, heat transfer, thermal chemistry, and electrochemistry on cell performance. The model outputs include spatial and temporal profiles of chemical composition, temperature, velocity, and current density. Mathematically the model forms a system of differential-algebraic equations (DAEs), which is solved computationally. The model is designed with process-control applications in mind, although it can certainly be applied more widely. Although the physical model is computationally efficient, it is still too costly for incorporation directly into real-time process control. Therefore, system-identification techniques are used to develop reduced-order, locally linear models that can be incorporated directly into advanced control methodologies, such as model predictive control (MPC). The paper illustrates the physical model and the reduced-order linear state-space model with examples.

1. Introduction

This paper is the first part of a two-paper sequence that discusses the incorporation of physical models into advanced process control. The present paper develops transient physical models for tubular solid-oxide fuel cell (SOFCs), and it discusses linear model-reduction strategies near certain steady-state operating points (OPs). The companion paper [1] concentrates on nonlinear reduced models and model predictive control (MPC) design.

The design and control of fuel-cell systems can benefit greatly from physically based models. The present paper is particularly concerned with models that can be applied to develop model-predictive process-control algorithms. In this application, high-fidelity transient response is required. The model considers flow and chemistry within a single anode-supported SOFC tube, as well as cathode air that flows over the external surfaces of a tubular stack. The approach is based generally upon earlier works [2–5]. However, to facilitate the real-time control applications, the models must be computationally fast and deliver accurate transient responses. To achieve computational efficiency, relatively coarse spatial discretization is used and heterogeneous reforming chemistry is modeled with global reactions. The charge-transfer chemistry is represented in a Butler–Volmer form that is derived from elementary reactions [6].

For process-control applications a pragmatic balance can be made between physical fidelity and computational efficiency. The primary objective of the model is to assist sensor interpretation and subsequent actuation. To achieve this objective, the model must incorporate all the relevant time scales associated with the physical and chemical processes. It must also represent the relationships between actuation and response. However, in practice the control actuation depends on feedback from sensors, albeit assisted by model-based interpretation. In other words, the control is not based upon model predictions directly. As discussed later in this paper, complex nonlinear physical models are further reduced to systems of linear state-space models that are incorporated into the control algorithms. Because the models that are incorporated into the control algorithms can be approximate, the underpinning physical models can approximate some physical attributes in return for computational speed.

2. Model development

Fig. 1 illustrates a prototype SOFC stack that is designed for a kilowatt-scale system. This stack contains 36 anode-supported tubular cells. Fuel enters the SOFC tubes from below and exits at the top of the stack. Cathode air enters radially at the bottom of the stack and leaves at the top through small clearances between the tubes and a top end plate. The physical model concentrates especially on the flow, chemistry, and thermal behaviors within the tubes. The air flow over the outsides of the tubes is modeled as a perfectly stirred reactor. The model accommodates heat

* Corresponding author. Tel.: +1 303 273 3379; fax: +1 303 273 3602.
E-mail address: rjkee@mines.edu (R.J. Kee).

0378-7753/$ – see front matter © 2010 Elsevier B.V. All rights reserved.
doi:10.1016/j.jpowsour.2010.06.074

Nomenclature

$A_{f,c}$	cross sectional area of fuel channel, m^2
A_s	cross sectional area of anode support layer, m^2
A_f	cross sectional area of anode functional layer, m^2
$A_{f,s}$	cross sectional area of anode support and functional layer, m^2
a_s	specific surface area of anode support layer, m^{-1}
a_f	specific surface area of anode functional layer, m^{-1}
B_g	permeability, m^2
c_p	heat capacity of the fuel channel flow, J kg^{-1} K^{-1}
$c_{p,m}$	heat capacity of the MEA, J kg^{-1} K^{-1}
d_p	particle diameter, m
$D^e_{k,Kn}$	effective Knudsen diffusion coefficients, m^2 s^{-1}
$D_{k\ell}$	binary diffusion coefficients, m^2 s^{-1}
$D^e_{k\ell}$	effective binary diffusion coefficients, m^2 s^{-1}
E^{eq}_a	reversible potential between the anode and electrolyte, V
E^{eq}_c	reversible potential between the cathode and electrolyte, V
E_{H_2}	activation energy for H_2 oxidation in the Butler–Volmer equation, J $kmol^{-1}$
E_{O_2}	activation energy for O_2 reduction in the Butler–Volmer equation, J $kmol^{-1}$
E_{cell}	cell potential, V
E_{rev}	reversible cell potential, V
F	Faraday constant, C $kmol^{-1}$
G°	standard state Gibbs free energy, J $kmol^{-1}$
h	enthalpy of the gas-phase mixtures, J kg^{-1}
h_k	species heat enthalpy, J kg^{-1}
h_q	heat transfer coefficient between fuel channel flow and MEA, W m^{-2} K^{-1}
$h_{q,c}$	heat transfer coefficient between air stream and MEA, W m^{-2} K^{-1}
i_{cell}	local current density, A m^{-2}
i_0	exchange current density for H_2 oxidation, A m^{-2}
$i^*_{H_2}$	nominal exchange current density of H_2 oxidation, A m^{-2}
i^*_{ref,H_2}	parameter $i^*_{H_2}$ at the reference temperature T_{ref}, A m^{-2}
$i_{0,c}$	exchange current density for O_2 reduction, A m^{-2}
$i^*_{O_2}$	nominal exchange current density of O_2 reduction, A m^{-2}
i^*_{ref,O_2}	parameter $i^*_{O_2}$ at the reference temperature T_{ref}, A m^{-2}
$\mathbf{j}_k$	gas-phase species mass flux, kg m^{-2} s^{-1}
$\mathbf{J}_k$	gas-phase species mole flux, kmol m^{-2} s^{-1}
$\mathbf{j}_{z,k}$	axial diffusive mass flux of k th species within the fuel channel flow, kg m^{-2} s^{-1}
$\mathbf{j}_{r,k}$	radial mass flux of k th species from the fuel flow into the porous anode, kg m^{-2} s^{-1}
$\mathbf{j}^c_{r,k}$	radial mass flux of k th species from the MEA into the air stream, kg m^{-2} s^{-1}
$\mathbf{j}^e_{r,k}$	radial mass flux of k th species from the anode functional layer into the electrolyte, kg m^{-2} s^{-1}
$\mathbf{j}^s_{r,k}$	radial mass flux of k th species from the anode support into the functional layer, kg m^{-2} s^{-1}
K	number of gas-phase species
n_e	number of charge transferred in the overall charge transfer reaction
Nu	Nusselt number of fuel channel flow
P_f	perimeter between the fuel channel and anode support layer, m
P_s	perimeter between the anode support layer and functional layer, m
P_e, P_c	perimeter between the MEA and air stream, m
p	pressure, Pa
p_{f,H_2}	partial pressure of H_2 within the anode functional layer, atm
p_{f,H_2O}	partial pressure of H_2O within the anode functional layer, atm
p_{a,O_2}	partial pressure of O_2 within the air stream, atm
$p^*_{H_2}$	parameter in the expression of i_0, atm
$p^*_{O_2}$	parameter in the expression of $i_{0,c}$, atm
q_{cond}	axial conductive heat flux within fuel channel flow, W m^{-2}
q_{diff}	axial heat flux within fuel channel flow from diffusion, W m^{-2}
q^a_{diff}	radial heat flux from the fuel channel flow into the anode from mass transport, W m^{-2}
q^c_{diff}	radial heat flux from the MEA into the air stream from mass transport, W m^{-2}
q_{mea}	axial conductive heat flux within the MEA, W m^{-2}
R	universal gas constant, J $kmol^{-1}$ K^{-1}
r_e	outer radius of anode functional layer, m
r_f	outer radius of fuel channel, m
r_p	pore radius, m
r_s	outer radius of anode support layer, m
$\dot{s}_k$	molar production rate by surface reactions, kmol m^{-2} s^{-1}
t	time, s
T	temperature of the fuel channel flow, K
T_a	temperature of the air stream, K
T_m	temperature of the composite MEA, K
UA_a	overall heat transfer coefficient between air stream and enclosure, W m^{-2} K^{-1}
V	volume of fuel channel flow control volume, m^3
W_k	species molecular weight, kg $kmol^{-1}$
$\overline{W}$	mean molecular weight, kg $kmol^{-1}$
X_k	gas-phase species mole fractions
$[X_k]$	gas-phase species molar concentrations, kmol m^{-3}
$[X_T]$	total gas-phase molar concentrations, kmol m^{-3}
Y_k	gas-phase species mass fractions within the fuel channel flow
$Y_{a,k}$	gas-phase species mass fractions within the air stream flow
$Y_{f,k}$	gas-phase species mass fractions within the anode functional layer
$Y_{s,k}$	gas-phase species mass fractions within the anode support layer
z	axial coordinate, m

Greek letters

α_a	anodic symmetric factor in the Butler–Volmer equation
α_c	cathodic symmetric factor in the Butler–Volmer equation
δz	axial length of fuel channel control volume, m
λ	heat conductivity of fuel channel flow, W m^{-1} K^{-1}
λ_m	heat conductivity of composite MEA, W m^{-1} K^{-1}
μ	gas-phase viscosity, kg m^{-1} s^{-1}
ν_k	reaction stoichiometry of species k in overall charge transfer reaction

ρ	gas-phase mass density of fuel channel flow, kg m^{-3}
ρ_f	gas-phase mass density within anode functional layer, kg m^{-3}
ρ_s	gas-phase mass density within anode support layer, kg m^{-3}
τ_g	tortuosity of the gas-phase
ϕ_g	porosity
ϕ_f	porosity of anode functional layer
ϕ_s	porosity of anode support layer
η	local overpotential, V
η_{act}	local activation overpotential, V
$\eta_{act,a}$	local activation overpotential within the anode, V
$\eta_{act,c}$	local activation overpotential within the cathode, V
η_{ohm}	local ohmic overpotential from ion conduction, V

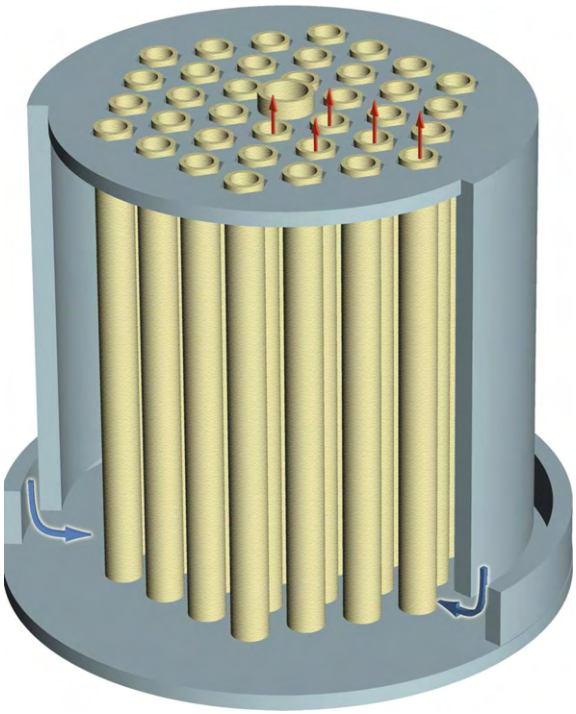

Fig. 1. A tubular SOFC stack consisting of three hexagonal rings of anode-supported cells.

and mass transfer between the tube exteriors and the cathode air.

The fuel-cell model is written in terms of small finite volumes along the length of an individual tube. Fuel flows within the tubes (anode side) and air circulates outside the tubes (cathode side). The fuel-flow models are based upon a plug-flow approximation in which only axial variations are modeled. That is, perfect mixing is assumed across the radius of the tube. When hydrocarbon fuels are used, reforming can proceed via catalytic chemistry within the anode support structure. Charge-transfer chemistry proceeds at the interfaces between the dense electrolyte and the composite electrode structures. The model accommodates heat transfer within the tubular structure and heat exchange between the tube and gases.

The following sections present derivations of the underpinning conservation equations for mass and energy. The derivations follow standard practice for deriving such equations based upon appropriate semi-differential control volumes. However, readers not familiar with such derivations may wish to consult a text on chemically reacting flow for details [7].

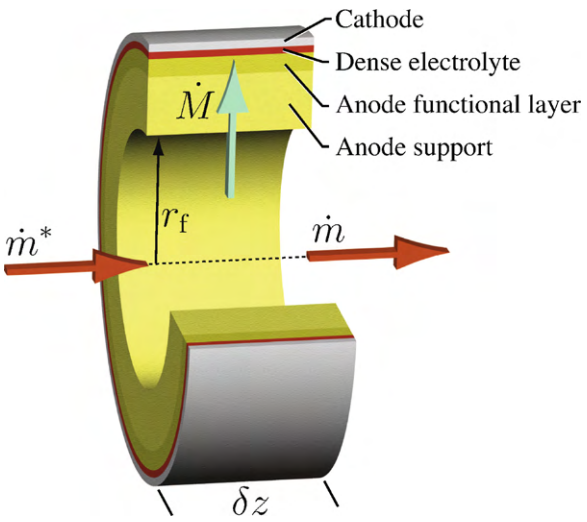

Fig. 2. Control volume annotated for the overall fuel-flow continuity equation.

2.1. Fuel flow, overall mass continuity

Fig. 2 illustrates a control volume for a short tube section. The mass-conservation equation for the flowing gases within tube is written as

$$\frac{d\rho}{dt} = \frac{\dot{m}^* - \dot{m} - \dot{M}}{V}, \tag{1}$$

where ρ is the mass density, $\dot{m}^*$ is the mass flow rate entering the control volume, $\dot{m}$ is the mass-flow rate leaving the control volume, and $\dot{M}$ is the mass-flow rate leaving the control volume and entering the porous-anode structure, and V is the volume of the control volume. Because the tube is segmented into small sections of length δz, the entering mass flow rate $\dot{m}^*$ is equal to the mass flow rate $\dot{m}$, which is leaving the adjacent upstream segment. The mass exchange between the fuel flow and the anode structure is represented as

$$\dot{M} = \sum_{k=1}^{K} j_{r,k} P_f \delta z, \tag{2}$$

where $j_{r,k}$ represents the radial mass flux of species k *from* the fuel flow *into* the porous anode structure. The fuel-tube perimeter is $P_f = 2\pi r_f$ and K is the total number of species.

A perfect-gas equation of state,

$$\rho = \frac{p\bar{W}}{RT} = \frac{p}{RT}\frac{1}{\sum_{k=1}^{K} Y_k/W_k}, \tag{3}$$

relates the density, pressure p, temperature T, and the mean molecular weight $\bar{W}$. The species mass fractions are Y_k and the molecular weights are W_k.

By differentiating the equation of state, the mass continuity equation can be rewritten to eliminate the mass-density derivative in favor of temperature and mass-fraction derivatives (pressure is assumed to be constant) as

$$\dot{m} = \dot{m}^* - \dot{M} + \frac{\rho V}{T}\frac{\partial T}{\partial t} + \rho V \bar{W} \sum_{k=1}^{K-1} \left(\frac{1}{W_k} - \frac{1}{W_K}\right) \frac{\partial Y_k}{\partial t}. \tag{4}$$

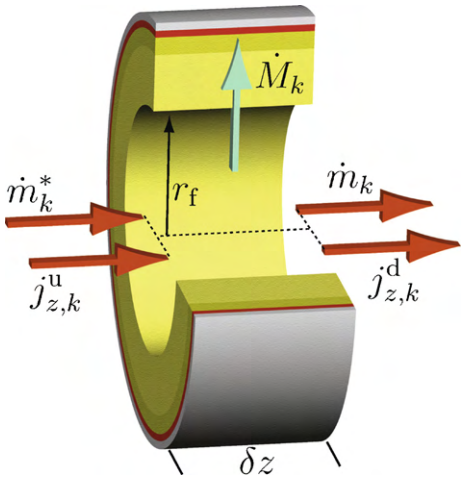

Fig. 3. Control volume annotated for the fuel-flow species continuity equations.

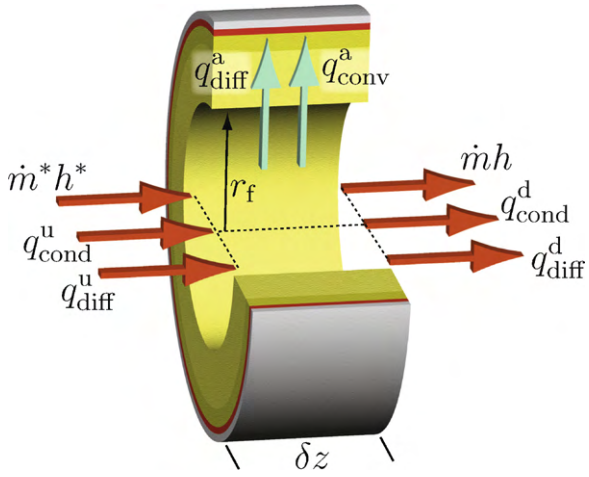

Fig. 4. Control volume annotated for the fuel-flow thermal energy equation.

The summation to $K-1$, not K, is because exact species conservation is enforced by $Y_K = 1 - \sum_{k=1}^{K-1} Y_k$. Because all the species mass fractions are not independent, the molecular weight W_K for species K appears in the last term.

2.2. Fuel flow, species continuity equations

Fig. 3 illustrates species fluxes into and out of a fuel channel control volume. The species continuity equation for the fuel flow within the tube may be written as

$$V\frac{\partial(\rho Y_k)}{\partial t} = \dot{m}_k^* - \dot{m}_k - \dot{M}_k + A_{f,c}\left(j_{z,k}^u - j_{z,k}^d\right). \tag{5}$$

In this equation, Y_k represents the mass fractions within the control volume, which are the same as the mass fractions leaving the control volume. The entering and exiting species mass flow rates are

$$\dot{m}_k^* = \dot{m}^* Y_k^*, \quad \dot{m}_k = \dot{m} Y_k, \tag{6}$$

where Y_k^* are the entering mass fractions. The rate of species mass exchange between the anode structure and the fuel channel is

$$\dot{M}_k = j_{r,k} P_f \delta z. \tag{7}$$

The axial diffusive mass fluxes across the upstream and downstream control surfaces are represented as $j_{z,k}^u$ and $j_{z,k}^d$, respectively. These axial fluxes are calculated using "mixture averaged" formulation [7]. The control-surface area is $A_{f,c} = \pi r_f^2$.

By substituting the overall mass-continuity equation (Eq. (1)) and some further algebraic manipulation, Eq. (5) can be rewritten as an explicit differential equation for the species mass fractions as

$$\begin{aligned}\frac{\partial Y_k}{\partial t} = {} & \frac{\dot{m}^*}{\rho V}\left(Y_k^* - Y_k\right) - \frac{1}{\rho V}\left(\dot{M}_k - Y_k\dot{M}\right) \\ & + \frac{A_{f,c}}{\rho V}\left(j_{z,k}^u - j_{z,k}^d\right), \quad (k = 1, \ldots, K-1).\end{aligned} \tag{8}$$

The mass fraction of the K th species is found as $Y_K = 1 - \sum_{k=1}^{K-1} Y_k$.

2.3. Fuel flow, thermal energy

As illustrated in Fig. 4, the energy equation has several contributing terms. In differential equation form,

$$\begin{aligned}\frac{\partial E}{\partial t} = {} & (\dot{m}^* h^* - \dot{m}h) \\ & + \left(q_{cond}^u - q_{cond}^d\right) A_{f,c} + \left(q_{diff}^u - q_{diff}^d\right) A_{f,c} \\ & - q_{diff}^a P_f \delta z - h_q (T - T_m) P_f \delta z.\end{aligned} \tag{9}$$

In this equation h is the specific enthalpy and $H = \rho V h$ is the total enthalpy. The internal energy time derivative $\partial E/\partial t$ is equal to the enthalpy time derivative because the pressure of the fuel channel flow is constant $\partial E/\partial t = \partial H/\partial t$. The first term on the right-hand side represents the energy convected into and out of the control volume. The second term represents thermal conduction. Using Fourier's law, the heat flux is represented as

$$q_{cond} = -\lambda\frac{\partial T}{\partial z}, \tag{10}$$

where λ is the thermal conductivity.

With the tube discretized into a series of control volumes, the temperature in each volume is represented as T. The upstream and downstream conduction are evaluated as

$$q_{cond}^u = -\lambda\frac{T - T^u}{\delta z}, \quad q_{cond}^d = -\lambda\frac{T^d - T}{\delta z}, \tag{11}$$

where T^u and T^d are the temperatures in the adjacent upstream and downstream control volumes. The third term in Eq. (9) represents the energy that is carried with the axial species diffusive fluxes across the control surfaces in the flow direction. Evaluating these terms depends upon the directions of the species fluxes as

$$q_{diff}^u = \begin{cases} \sum_{k=1}^{K} j_{z,k}^u h_k(T^u), & j_{z,k}^u > 0. \\ \sum_{k=1}^{K} j_{z,k}^u h_k(T), & j_{z,k}^u < 0. \end{cases} \tag{12}$$

If the upstream diffusion flux is into the control volume (i.e., $j_{z,k}^u > 0$), then the species enthalpy is evaluated at the temperature of the upstream control volume [i.e., $h_k(T^u)$]. If the upstream diffusion flux is out of the control volume (i.e., $j_{z,k}^u < 0$), then the species enthalpy is evaluated at the temperature of the target control volume [i.e., $h_k(T)$]. An analogous evaluation pertains to the

downstream diffusion flux,

$$q^{\mathrm{d}}_{\mathrm{diff}} = \sum_{k,j^{\mathrm{d}}_{z,k}>0}^{K} j^{\mathrm{d}}_{z,k} h_k(T) + \sum_{k,j^{\mathrm{d}}_{z,k}<0}^{K} j^{\mathrm{d}}_{z,k} h_k(T^{\mathrm{d}}). \tag{13}$$

The fourth term in Eq. (9) represents the thermal energy that is transferred between the porous anode and the fuel flow as a result of mass exchange. That is,

$$q^{\mathrm{a}}_{\mathrm{diff}} = \begin{cases} \sum_{k=1}^{K} j_{r,k} h_k(T), & j_{r,k} > 0. \\ \sum_{k=1}^{K} j_{r,k} h_k(T_{\mathrm{m}}), & j_{r,k} < 0. \end{cases} \tag{14}$$

Because when $j_{r,k} > 0$ species k is transported from the fuel flow into the anode structure, the species enthalpy is evaluated at the fuel-flow temperature [i.e., $h_k(T)$]. When $j_{r,k} < 0$ species k is transported from the anode structure into the fuel flow and species enthalpy is evaluated at the membrane-electrode assembly (MEA) temperature [i.e., $h_k(T_{\mathrm{m}})$]. The fifth term in Eq. (9) represents the thermal energy that is transferred by fluid convection between the anode surface and the fuel flow. This term is evaluated using Newton's law of cooling, where the heat-transfer coefficient h_{q} is evaluated from a Nusselt-number correlation as

$$h_{\mathrm{q}} = \frac{\lambda \mathrm{Nu}}{2 r_{\mathrm{f}}}. \tag{15}$$

For the laminar flows that are typical in small tubular fuel cells, the approximate Nusselt number is Nu = 3.66. After substituting the mass-continuity equation and some algebraic manipulation, the fuel-flow energy equation can be written as a differential equation for the gas temperature as

$$\begin{aligned} c_p \frac{\partial T}{\partial t} = & \frac{\dot{m}^*}{\rho V}(h^* - h) + \frac{\dot{M}}{\rho V} h \\ & + \left(q^{\mathrm{u}}_{\mathrm{cond}} - q^{\mathrm{d}}_{\mathrm{cond}}\right) \frac{A_{\mathrm{f,c}}}{\rho V} \\ & + \left(q^{\mathrm{u}}_{\mathrm{diff}} - q^{\mathrm{d}}_{\mathrm{diff}}\right) \frac{A_{\mathrm{f,c}}}{\rho V} \\ & - q^{\mathrm{a}}_{\mathrm{diff}} \frac{P_{\mathrm{f}}}{\rho V} \delta z + h_{\mathrm{q}} (T_{\mathrm{m}} - T) \frac{P_{\mathrm{f}}}{\rho V} \delta z \\ & - \sum_{k=1}^{K-1} (h_k - h_K) \frac{\partial Y_k}{\partial t}. \end{aligned} \tag{16}$$

Because all species mass fractions are not independent, splitting the time derivative of specific energy into temperature and composition contributions causes the specific enthalpy h_K of species K to appear in the last term.

2.4. Anode bi-layer model

Fig. 5 illustrates the structure and notation for mass balances within the porous composite anode structure. The model divides the anode structure into two layers, the support layer and the functional layer. Both layers are typically the same composition (e.g., Ni-YSZ). The support layer is relatively thick (e.g., 500–1000 μm) and has relatively open porosity. There can be considerable catalytic reforming chemistry within the support layer, but essentially no charge-transfer chemistry. The functional layer is relatively thin (e.g., 20–50 μm), with large three-phase-boundary (TPB) lengths and relatively small particle and pore spaces. The primary role of the functional layer is to facilitate charge-transfer chemistry near the dense electrolyte.

The radius of the interface between the support and functional layers is r_{s} and the radius of the interface between the functional layer and the dense electrolyte is r_{e}. The average gas-phase compositions within the pore spaces of the support and functional layers are represented by mass fractions as $Y_{\mathrm{s,k}}$ and $Y_{\mathrm{f,k}}$, respectively. Porosity of the anode support layer is represented as ϕ_{s} and the specific catalyst surface area (i.e., effective are per unit volume) is represented as a_{s}. Radial mass fluxes of gas-phase species at the interface between the support and fuel channel are represented as $j_{r,k}$, radial gas-phase fluxes at the interface between the support and functional layer are represented as $j^{\mathrm{s}}_{r,k}$, and radial gas-phase fluxes at the interface between the functional layer and the dense electrolyte are represented as $j^{\mathrm{e}}_{r,k}$. Axial transport within the anode structure is negligible because the radial gradients are significantly greater.

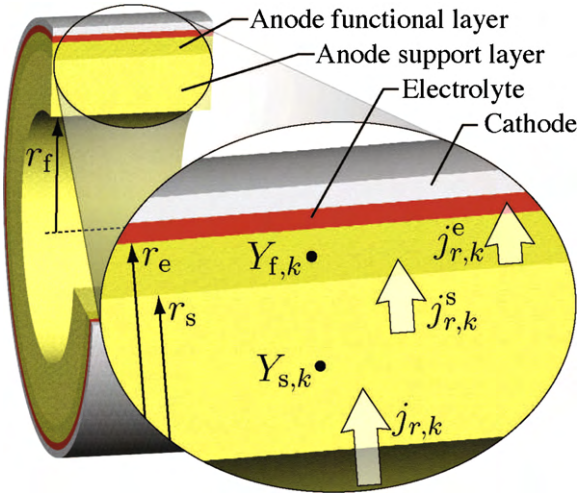

Fig. 5. Control volume annotated for the bi-layer composite anode structure.

The species mass-continuity equations within the anode support layer are written as

$$\frac{\partial}{\partial t}(\phi_{\mathrm{s}} \rho_{\mathrm{s}} Y_{\mathrm{s,k}}) = \left(a_{\mathrm{s}} \dot{s}_k + \frac{P_{\mathrm{f}}}{A_{\mathrm{s}}} j_{r,k} - \frac{P_{\mathrm{s}}}{A_{\mathrm{s}}} j^{\mathrm{s}}_{r,k}\right) W_k, \tag{17}$$

where $\dot{s}_k$ are the molar production rates of species via heterogeneous catalytic chemistry. The average gas-phase density within the pores of the anode support is ρ_{s}. The perimeter $P_{\mathrm{f}} = 2\pi r_{\mathrm{f}}$ is the perimeter between the fuel channel and the support layer. The perimeter $P_{\mathrm{s}} = 2\pi r_{\mathrm{s}}$ is the perimeter between the support layer and the functional layer. The axial cross-sectional area of the anode support is $A_{\mathrm{s}} = \pi(r_{\mathrm{s}}^2 - r_{\mathrm{f}}^2)$. The overall mass continuity equation for the support layer, which is found by summing the species continuity equations over all species, is written as

$$\frac{\partial}{\partial t}(\phi_{\mathrm{s}} \rho_{\mathrm{s}}) = \sum_{k=1}^{K} \left(\frac{P_{\mathrm{f}}}{A_{\mathrm{f}}} j_{r,k} - \frac{P_{\mathrm{s}}}{A_{\mathrm{s}}} j^{\mathrm{s}}_{r,k}\right) W_k. \tag{18}$$

This continuity equation is formed assuming no surface species are involved in the heterogeneous reactions.

The species mass-continuity equations within the anode functional layer are analogous to those for the support layer. That is,

$$\frac{\partial}{\partial t}(\phi_{\mathrm{f}} \rho_{\mathrm{f}} Y_{\mathrm{f,k}}) = \left(a_{\mathrm{f}} \dot{s}_k + \frac{P_{\mathrm{s}}}{A_{\mathrm{f}}} j^{\mathrm{s}}_{r,k} - \frac{P_{\mathrm{e}}}{A_{\mathrm{f}}} j^{\mathrm{e}}_{r,k}\right) W_k. \tag{19}$$

The specific surface area a_{f} and porosity ϕ_{f} of the functional layer may be different from that in the support layer. The perimeter at the dense-electrolyte interface is $P_{\mathrm{e}} = 2\pi r_{\mathrm{e}}$ and the axial cross-sectional area is $A_{\mathrm{f}} = \pi(r_{\mathrm{e}}^2 - r_{\mathrm{s}}^2)$. The overall continuity equation for

gases within the functional layer is

$$\frac{\partial}{\partial t}(\phi_f \rho_f) = \sum_{k=1}^{K} \left(\frac{P_s}{A_f} j^s_{r,k} - \frac{P_e}{A_f} j^e_{r,k} \right) W_k. \tag{20}$$

The heterogeneous reforming chemistry is based upon global reactions for steam reforming of methane, water-gas-shift (WGS), and partial oxidation of methane.

$$CH_4 + H_2O \rightleftharpoons CO + 3H_2, \tag{21}$$

$$CO + H_2O \rightleftharpoons CO_2 + H_2, \tag{22}$$

$$CH_4 + \frac{1}{2}O_2 \rightleftharpoons CO + 2H_2. \tag{23}$$

The rates of these global reactions were approximated by fitting to experimental data for methane reforming as measured in a separated anode experiment [8].

Three radial mass fluxes must be evaluated within the anode structure. The flux between the support and the fuel flow $j_{r,k}$ and the flux between the functional layer and the support layer $j^s_{r,k}$ are evaluated using the dusty-gas model (DGM) [9,2]. The DGM provides an implicit relationship among the gas-phase species molar fluxes through the porous matrix $\mathbf{J}_k$, molar concentrations $[X_k]$, concentration gradients, and the pressure p gradient as,

$$\begin{aligned} &\sum_{\ell \neq k} \frac{[X_\ell]\mathbf{J}_k - [X_k]\mathbf{J}_\ell}{[X_T] D^e_{k\ell}} + \frac{\mathbf{J}_k}{D^e_{k,Kn}} \\ &= -\nabla[X_k] - \frac{[X_k]}{D^e_{k,Kn}} \frac{B_g}{\mu} \nabla p, \end{aligned} \tag{24}$$

where $[X_T] = p/RT$ is the total molar concentration, B_g is the permeability, and μ is the mixture viscosity. The mass fluxes $\mathbf{j}_k$ are related simply to the molar fluxes $\mathbf{J}_k$ as $\mathbf{j}_k = W_k \mathbf{J}_k$. Knudsen diffusion represents mass transport assisted by gas-wall collisions. The Knudsen diffusion coefficients depend upon the porous-media microstructure, including porosity, average pore radius r_p, and tortuosity τ_g. The effective binary and Knudsen diffusion coefficients $D^e_{k\ell}$ and $D^e_{k,Kn}$ can be evaluated as

$$D^e_{k\ell} = \frac{\phi_g}{\tau_g} D_{k\ell}, \quad D^e_{k,Kn} = \frac{2}{3} \frac{r_p \phi_g}{\tau_g} \sqrt{\frac{8RT}{\pi W_k}}. \tag{25}$$

The binary diffusion coefficients $D_{k\ell}$ and the mixture viscosities μ are determined from kinetic theory [7]. The permeability can be evaluated from the Kozeny–Carman relationship as

$$B_g = \frac{\phi_g^3 d_p^2}{72 \tau_g (1-\phi_g)^2}, \tag{26}$$

where d_p is the particle diameter. Further details of the DGM and its numerical implementation can be found in Zhu, et al. [2]. The two fluxes $j_{r,k}$ and $j^s_{r,k}$ are evaluated based on the transport properties of the anode support.

The mass fluxes at the interface between the anode functional layer and the dense electrolyte $j^e_{r,k}$ are determined by the charge-transfer chemistry

$$j^e_{r,k} = -\frac{\nu_k i_{cell}}{n_e F} W_k, \tag{27}$$

where i_{cell} is the current density and F is Faraday's constant. The variables ν_k and n_e are the stoichiometric coefficient for species k and number of electrons transferred in the overall charge transfer reaction.

2.5. MEA energy balance

The entire thickness of the MEA is represented by a single temperature T_m, which varies temporally and axially. As illustrated in Fig. 6, heat enters and exits the MEA through conduction, mass transport, and convection. The energy balance for the MEA is written as

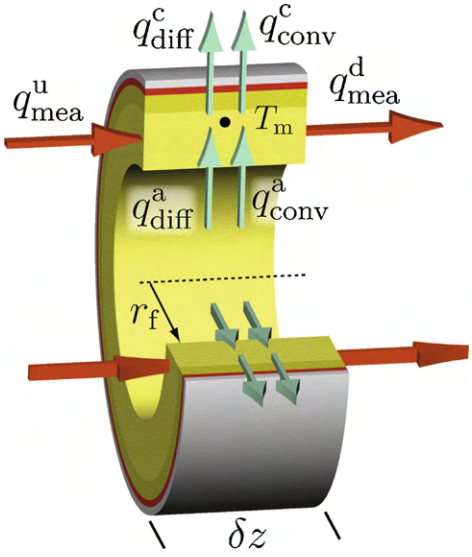

Fig. 6. Control volume annotated for the thermal balance in the MEA, which is the entire tube wall.

$$\begin{aligned} (1-\phi_m) \quad \frac{\partial(\rho_m c_{p,m} T_m)}{\partial t} &= \left(q^u_{mea} - q^d_{mea}\right) \frac{1}{\delta z} \\ &+ \frac{P_f}{A_{f,s}} \sum_{k=1}^{K} j_{r,k} h_k - \frac{P_e}{A_{f,s}} j^c_{r,O_2} h_{O_2} \\ &+ \frac{P_f}{A_{f,s}} h_q (T - T_m) - \frac{P_e}{A_{f,s}} h_{q,c} (T_m - T_a) \\ &- \frac{P_e}{A_{f,s}} E_{cell} i_{cell}, \end{aligned} \tag{28}$$

where $A_{f,s}$ is the combined cross sectional area of the anode support and functional layer. The first term on the right-hand side represents axial thermal conduction through the solid materials that comprise the MEA. The upstream and downstream conduction terms are evaluated as

$$q^u_{mea} = -\lambda_m \frac{T_m - T^u_m}{\delta z}, \quad q^d_{mea} = -\lambda_m \frac{T^d_m - T_m}{\delta z}, \tag{29}$$

where T^u_m and T^d_m are the MEA temperatures in the adjacent upstream and downstream control volumes and λ_m is the effective thermal conductivity of the MEA. The MEA porosity ϕ_m is an area average of anode-support and anode-functional layers porosity. The second term on the right-hand side of Eq. (28) represents the energy that is transported via species flux from the fuel stream to the anode support layer. The third term represents the energy that is transported via species flux from the cathode to the exterior. As discussed in the context of the fuel-flow energy balance (e.g., Eq. (14)), the temperature at which the enthalpy is evaluated depends upon the direction of the species flux. In a similar way, energy exchange between the cathode and the exterior is evaluated as

$$q^c_{diff} = \begin{cases} \displaystyle\sum_{k=1}^{K} j^c_{r,k} h_k(T_m), & j^c_{r,k} > 0 \\ \displaystyle\sum_{k=1}^{K} j^c_{z,k} h_k(T_a), & j^c_{r,k} < 0 \end{cases} \tag{30}$$

Because when $j^c_{r,k} > 0$ species k is transported from the cathode into the surrounding air stream, the species enthalpy is evaluated

at the MEA temperature [i.e., $h_k(T_m)$]. When $j^c_{r,k} < 0$ species k is transported from the surrounding air stream and species enthalpy is evaluated at the air stream temperature [i.e., $h_k(T_a)$].

The fourth and fifth terms in Eq. (28) represent convective heat transfer between the MEA and adjacent gas flows. The heat-transfer coefficients on the exterior cathode side $h_{q,c}$ is an empirical parameter. The final term in Eq. (28) represents the electrical energy produced by the cell, which does not contribute to the thermal energy balance. Assuming that the dense electrolyte and cathode are very thin, the cathode perimeter is $P_c = P_e = 2\pi r_e$.

2.6. Cathode air conservation equations

The model is based upon an assumption that the cathode air that circulates around the outsides of the tube stack behaves as a perfectly stirred reactor. That is, the air temperature and composition may vary temporally, but are uniform spatially. The rate at which oxygen is transferred from the circulating air to the SOFC cathodes depends upon the cell operating conditions. Heat is exchanged between the tubes and the air by convection and by the energy associated with the oxygen mass transfer.

The species continuity equation for the cathode air is written as

$$V_a \frac{d(\rho Y_{a,k})}{dt} = \dot{m}^*_a Y^*_{a,k} - \dot{m}_a Y_{a,k}, \quad k \neq O_2, \tag{31}$$

where $\dot{m}^*_a$ is the mass flow rate of the inlet air and $Y^*_{a,k}$ are the inlet species mass fractions (usually only O_2 and N_2). The mixture within the volume V_a of cathode space and the exhaust flow are assumed to have the same composition, $Y_{a,k}$. The oxygen mass fraction is determined from $Y_{a,O_2} = 1 - \sum_{k \neq O_2}^{K} Y_{a,k}$. The overall mass-continuity equation is

$$V_a \frac{d\rho}{dt} = \dot{m}^*_a - \dot{m}_a - \dot{M}_a, \tag{32}$$

where $\dot{M}_a$ is the oxygen mass-consumption rate by the SOFC stack.

The cathode-air energy equation is

$$\begin{aligned} V_a \frac{d(\rho e)}{dt} = {} & \dot{m}^*_a h^*_a - \dot{m}_a h_a - UA_a(T_a - T_{shell}) \\ & + P_e \int_0^L h_{q,c}(T_m - T_a)dz \\ & + P_e \int_0^L j_{r,O_2} h_{O_2} dz. \end{aligned} \tag{33}$$

The first two terms on the right-hand side represent the energy associated with the air flow into and out of the cathode-air compartment. The third term, which represents heat transfer from the cathode air to the surrounding enclosure, uses an overall heat transfer coefficient UA_a. The fourth term is an integral that represents the convective heat transfer along the length L of an SOFC tube to the surrounding air. The final term represents the energy associated with oxygen mass exchange between the SOFC cathode and the surrounding air.

2.7. Electrochemistry

The first step in modeling the electrochemistry is to determine the cell voltage E_{cell}. The cell voltage is equal to the reversible voltage minus the sum of various overpotentials

$$E_{cell} = E_{rev} - \eta_{act,a} + \eta_{act,c} - \eta_{ohm}, \tag{34}$$

where E_{rev} is the reversible voltage (cell voltage when no net current is produced). The ohmic overpotential η_{ohm} is mainly from ion conduction through the electrolyte. There is an activation overpotential to drive charge-transfer chemistry at the cathode $\eta_{act,c}$ and the anode $\eta_{act,a}$. Because each of the overpotentials depends upon current density, Eq. (34) can be used to determine the local current density for each discrete control volume along the length of the SOFC tube. Because the model determines the composition in the anode functional layer, there is no need to include concentration overpotentials.

The reversible voltage is calculated based on the global charge-transfer reactions at the anode and cathode side being in local equilibrium. On the cathode, oxygen from the air stream is reduced by reaction with electrons, producing an oxygen ion in the electrolyte as

$$\frac{1}{2}O_2(g) + 2e^-(c) \rightleftharpoons O^{2-}(el). \tag{35}$$

The oxygen ion is transported across the dense electrolyte toward the anode functional layer. Within the anode functional layer, hydrogen from the fuel stream reacts with the oxygen ion and delivers electrons into the anode phase as

$$H_2(g) + O^{2-}(el) \rightleftharpoons H_2O(g) + 2e^-(a). \tag{36}$$

The overall reversible potential can be calculated by setting the electrochemical energy change for reactions (35) and (36) to zero. The result is

$$E_{rev} = -\frac{\Delta G^o}{2F} + \frac{RT_m}{2F} \ln\left(\frac{p_{f,H_2} p^{1/2}_{a,O_2}}{p_{f,H_2O}}\right), \tag{37}$$

$$\Delta G^\circ = G^\circ_{f,H_2O} - \left(G^\circ_{f,H_2} + \frac{1}{2}G^\circ_{a,O_2}\right), \tag{38}$$

where $p_{k,f}$ and $p_{k,a}$ are the partial pressures (evaluated in atm) of species k in the anode functional layer and air stream, respectively. The standard state Gibbs free energy change G° is only a function of temperature and not concentration. Thus, the first term in Eq. (37) accounts for temperature effects. The last term accounts for composition and pressure effects.

Butler–Volmer equations are used to determine the local current density i at the anode and cathode side for a given activation overpotential

$$i = i_0\left(\exp\left(\frac{\alpha_a F \eta_{act}}{RT_m}\right) - \exp\left(-\frac{\alpha_c F \eta_{act}}{RT_m}\right)\right). \tag{39}$$

The exchange current density is a function of the local concentrations and temperature at the TPBs. The global anodic and cathodic symmetry factors α_a and α_c do not necessarily sum to one. For a given charge-transfer reaction mechanism, the functional form of the exchange current density and global symmetry factors are derived by assuming one elementary reaction is rate limiting and that all other reactions are in partial equilibrium.

The assumed hydrogen oxidation mechanism and rate limiting step are taken from Zhu et al. [2]. By assuming the symmetry factors for the elementary rate limiting step are both $\alpha_a = \alpha_c = 0.5$, the functional form of the exchange current density for the electrochemical oxidation of hydrogen is

$$i_0 = i^*_{H_2} \frac{(p_{f,H_2}/p^*_{H_2})^{1/4}(p_{f,H_2O})^{3/4}}{1 + (p_{f,H_2}/p^*_{H_2})^{1/2}}, \tag{40}$$

where $i^*_{H_2}$ and $p^*_{H_2}$ are only functions of temperature. Also, the global symmetry factors for hydrogen oxidation are $\alpha_a = 1.5$ and $\alpha_c = 0.5$. For the cathode, the mechanism for the electrochemical reduction of oxygen is also taken from Zhu et al. [2]. Based on the assumed elementary rate limiting step having symmetry factors equal to 0.5, the exchange current density for the cathode side is

$$i_{0,c} = i^*_{O_2} \frac{(p_{a,O_2}/p^*_{O_2})^{1/4}}{1 + (p_{a,O_2}/p^*_{O_2})^{1/2}}. \tag{41}$$

The global symmetry factors for the electrochemical reduction of oxygen are $\alpha_a = 0.5$ and $\alpha_c = 0.5$. The nominal exchange current densities i^* depend on temperature in the following way

$$i_e^* = i_{ref,e}^* \exp\left(-\frac{E_e}{R}\left(\frac{1}{T} - \frac{1}{T_{ref}}\right)\right) \quad (42)$$

where "e" represents the electrochemical oxidation of oxygen or hydrogen. The parameter $i_{ref,e}^*$ is the nominal exchange current density at the reference temperature T_{ref}. It is important to note that all partial pressures in Eqs. (40) and (41) must be evaluated in atmospheres.

3. Implementation

Spatial derivatives are evaluated using the finite volume method. The resulting governing equations from a set of differential-algebraic equations (DAEs) [10]. The model is implemented in C++ and linked to SUNDIALS[11] and CANTERA[12]. The discretized equations are solved using the DAE solver IDA contained within SUNDIALS. Based on mesh studies, an axial mesh of 100 points accurately captures spatial variation along the tube. For each axial mesh point, there is an anode support layer, anode functional layer, and fuel channel control volume. The chemically reacting flow software CANTERA is utilized to calculate fluxes within the anode according to the DGM. CANTERA is also used to evaluate thermodynamic properties, transport properties, and net rates of production from thermal chemistry.

4. Example model results

A specific anode-supported SOFC tube is used to illustrate the model. The 15 cm long tube with an outside diameter of 1 cm., is typical of a tube that may be used in a sub-kilowatt tubular stack. Table 1 lists other model parameters, describing physical and electrochemical characteristics. Most of these parameters are taken from Zhu et al. [4]. The effective thermal conductivity of the composite MEA (i.e., tube wall) is approximated as $\lambda_m = 10.5$ W m^{-1} K^{-1}[13]. The nominal exchange current densities $i_{H_2}^* = 2.07$ A cm^{-2} and $i_{O_2}^* = 0.68$ A cm^{-2} were adjusted such that model predicted power densities match those of typical small scale systems (around 0.3 W cm^{-2} for fuel utilization of around 85%).

Table 1
Model parameters for a single tube. Many of the parameters are from Zhu et al. [4].

Parameter	Value
Thermal properties	
MEA thermal conductivity, λ_m (W m^{-1} K^{-1})	10.5
MEA porosity, ϕ_m	0.35
MEA heat capacity, $c_{p,m}$ (J kg^{-1} K^{-1})	533
MEA density, ρ_m (kg m^{-3})	7000
Nominal heat transfer coefficient, $h_{q,c}$ (W m^{-2} K^{-1})	120
Nominal overall heat transfer coefficient, UA_a (W K^{-1})	0.85
Nusselt number, $Nu_D = h_q P_f/(\pi\lambda)$	3.66
Anode support layer properties	
Thickness, L_s (μm)	950
Porosity, ϕ_s	0.35
Tortuosity, τ	3.5
Pore radius, r_p (μm)	0.5
Mean particle diameter, d_p (μm)	2.5
Specific catalyst area, a_s (m^{-1})	1.08e5
Anode functional layer properties	
Thickness, L_f (μm)	50
Porosity, ϕ_f	0.35
Specific catalyst area, a_f (m^{-1})	2.08e5
Nominal exchange current density, $i_{H_2}^*$ (A m^{-2})	2.07
Activation energy, E_{H_2} (kJ mol^{-1})	120
Reference temperature, T_{ref} (°C)	800
Electrolyte ohmic resistance $R = R_o T \exp(E_{ion}/(RT))$	
Activation energy, E_{ion} (kJ mol^{-1})	80
Resistance prefactor, R_o (Ωm^2 K^{-1})	5.55e-13
Cathode properties	
Nominal exchange current density, $i_{O_2}^*$ (A m^{-2})	0.68
Activation energy, E_{O_2} (kJ mol^{-1})	130
Reference temperature, T_{ref} (°C)	800

For purposes of illustrating the model, the inlet fuel composition is 38% H_2, 3% H_2O, 1% CH_4, 19% CO, 0.3% CO_2, and 38% N_2. This is the equilibrium mixture for methane and air at 800°C with a stochiometric ratio to partial oxidation (i.e., oxygen to carbon ratio of 0.5). A small amount of steam (3%) has been added to the equilibrium mixture. Fuel enters the tube at 800 °C and atmospheric pressure. The cathode air, which flows around the outsides of the tubes, enters the stack at 550°C. Both ends of the tubes conduct heat to manifolds at a fixed temperature of 800°C.

4.1. Steady-state results

Fig. 7 illustrates steady-state spatial profiles for composition, current density, temperature and fuel velocity with the cell operating at $E_{cell} = 0.72$ V. The fuel inlet velocity is 38 cm s^{-1}, and the air flow rate (per tube) is 33.5 mg s^{-1}. The total current and power produced by a single tube are 23.1 A and 16.6 W, respectively, which corresponds to current and power densities of 0.49 A cm^{-2} and 0.35 W cm^{-2}. Under these conditions, the cell achieves an efficiency of 49.9% and fuel utilization of 89.9%.

The fuel composition profiles (Fig. 7) are primarily driven by the electrochemical consumption of hydrogen. The ratio of hydrogen to steam decreases along the length of the cell due to current production. The heterogeneous WGS process (Eq. (22)) remains near equilibrium. Thus, carbon monoxide and steam react rapidly, replenishing the electrochemically consumed hydrogen. Overall, these processes consume hydrogen and carbon monoxide, producing steam and carbon dioxide. The small amount of methane (1%) entering the tube is quickly reformed by steam (Eq. (21)) to produce CO and H_2. Because this reaction increases moles, the nitrogen mole fraction decreases slightly. The methane steam reforming also produces a slight maximum in the velocity. The peak in the temperature profile is the result of internal heat generation and fixing the end temperatures.

Fig. 7 illustrates some interesting effects of temperature and fuel composition on local current density. Near the tube inlet, the cur-

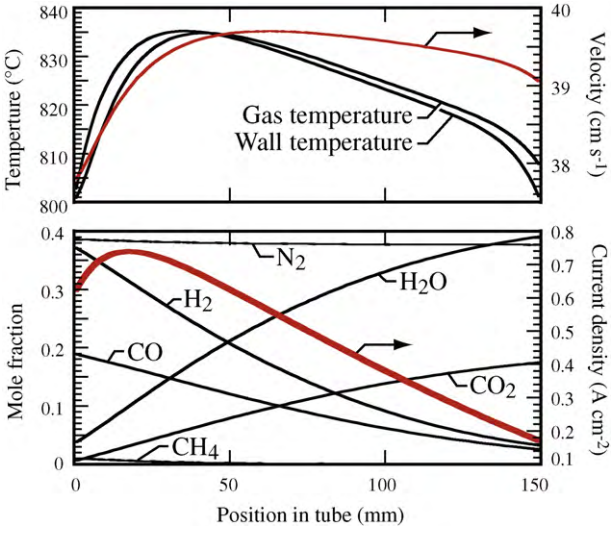

Fig. 7. Steady-state profiles for temperature, fuel channel composition, current density, and fuel velocity along the length of the cell. The cell voltage, fuel inlet velocity, and air mass flow rate are 0.72 V, 38 cm s^{-1} and 33.5 mg s^{-1}, respectively.

rent density increases. The current density reaches a maximum of 0.74 A cm^{-2} about 2 cm downstream of the inlet. Following the maximum, the current density decreases monotonically to around 0.17 A cm^{-2} at the fuel outlet. The reversible potential decreases along the tube as hydrogen is electrochemically consumed and steam is produced, tending to reduce the local current density. However, the current density also depends upon the local MEA temperature, which is maximum at around 3.5 cm from the tube entrance. These competing effects lead to the maximum current density occurring between the fuel inlet and maximum MEA temperature.

4.2. Transient simulations

The model is designed to run simulations with time-varying inputs. For instance, the cell voltage, fuel inlet velocity, and air flow rate can be adjusted to meet varying power demands. Consequently, the spatial profiles (composition, velocity, current density, etc.) are transient. However, the sensors are assumed to be positioned to measure tube-exhaust conditions. Thus, the controller is more concerned with the temporal variation of the outlet flows, average MEA temperature, and total current production than the spatial variations within the tube.

Consider the transient behavior that results in going from a low current demand to a high current demand. One second into the simulation, the current demand goes from 14.5 A to 30 A. At the start of the simulation, the cell is operating in steady state with a cell voltage of $E_{cell} = 0.78$ V, producing 11.3 W. The inlet fuel velocity is 25 cm s^{-1} and air flow rate is 33.5 mg s^{-1}. Under these conditions, the cell is operating at 52.3% efficiency and a fuel utilization of 87.2%. Figs. 8 and 9 illustrate transient response on short (seconds) and long (minutes) time scales, respectively.

One second after the start of the simulation, the current demand is increased from 14.5 A to 30 A. In an attempt to achieve the new current demand, the cell voltage is reduced from $E_{cell} = 0.78$ V to $E_{cell} = 0.69$ V. Lowering the cell voltage further could permanently degrade the tube. The voltage drop causes a sharp current increase from 14.5 A to around 25 A. The electrochemical charge-transfer rate responds instantly to the change in cell voltage. However, the suddenly increased current production increases fuel consumption, causing a subsequent decrease in current (Fig. 8). Thus, the new current demand of 30 A is not met with only a change in cell voltage. Also, the fuel utilization approaches 100% (i.e., very low H_2 in the exhaust), which is an undesirable condition. To meet the current demand of 30 A and offset fuel depletion, the fuel inlet velocity is increased from 24.7 cm s^{-1} to 51.4 cm s^{-1} over a half-second ramp beginning at 1.2 s. The increased fuel flow causes the current to increase to around 28 A and the H_2 in the exhaust increases to around 7% by around 2 s. Based upon the characteristic flow and diffusion times, the response time for rapid changes in operating conditions is around 1 s.

Beginning at 2 s after the start of simulation, the current increases on a shallow linear ramp toward and above the desired value of 30 A. With the voltage and inlet velocity held fixed, the fuel consumption increases leading to a decrease in the H_2 exhaust mole fraction (Fig. 8). During the first 10 s, the tube temperature, fuel-exhaust temperature, and cathode air temperature all increase slightly. The temperature rise is the result of increasing polarization losses as the cell power output increases.

Fig. 9 shows cell behavior on a longer time scale extending to 160 s. After 60 s, the current continues to rise above the demanded value of 30 A due to a continued rise in temperatures. The increased current and increased temperature cause increased fuel consumption. If the tube temperature becomes sufficiently high for a long period of time, then the tube might be permanently damaged. To

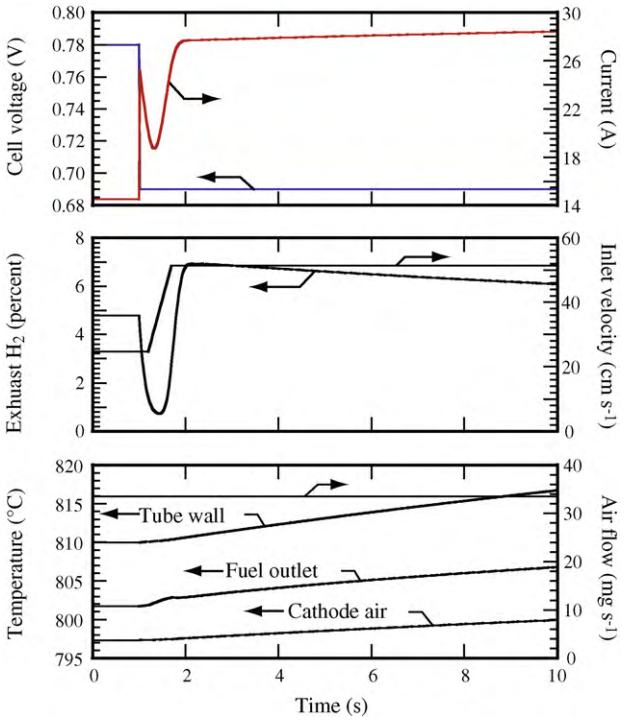

Fig. 8. Total current, exhaust H_2 mole fraction, and temperatures as functions of time, following a transient from a relatively low power to high power demand. The change is effected by reducing the cell voltage from 0.78 V to 0.69 V one second after the start of simulation. The velocity of the fuel inlet is increased from 24.7 cm s^{-1} to 51.4 cm s^{-1} over a half-second ramp beginning at 1.2 s after the start of simulation. The responses on the short time scale are characterized by the fluid-flow dynamics that are on the order of seconds.

stabilize the current production at 30 A and lower the average tube temperature, at around 80 s the cathode air flow rate is increased. The cooling effect of the cathode air serves to decrease tube and flow temperatures, although on relatively long time scales. The average tube temperature decreases and stabilizes at 830 ° C. The tube current stabilizes at 29.9 A. As the temperatures decrease, the fuel-consumption rate decreases (H_2 in exhaust increases) and the total current decreases slightly. At the end of simulation (160 s), the cell is operating with an efficiency of 45.9% with a fuel utilization of 85.9%.

This simulation illustrates the need for control of fuel cell systems to quickly meet varying current demands and not violate constraints. The desired higher current demand was only met and stabilized after 100 s, which is not acceptable. Also, the current was stabilized at a value 0.1 A below the desired value of 30 A. After the cell voltage decrease, the fuel outlet became almost completely starved of hydrogen and carbon monoxide. This could lead to damage of the tube. Often the fuel channel outlet stream is combusted in a tail gas combustor to provide required heat for the fuel cell system. The lean outlet condition experienced during the simulation could cause the flame in tail gas combustor to extinguish.

5. Linear identification of the SOFC stack

The physical model contains the coupled effects of fuel channel flow, porous-media transport, heat transfer, reforming chemistry, and electrochemistry. Although already simplified compared to even-more-complex physical models, the required computational resources are still too great for direct incorporation into an MPC implementation [14]. Although the physical model is highly non-

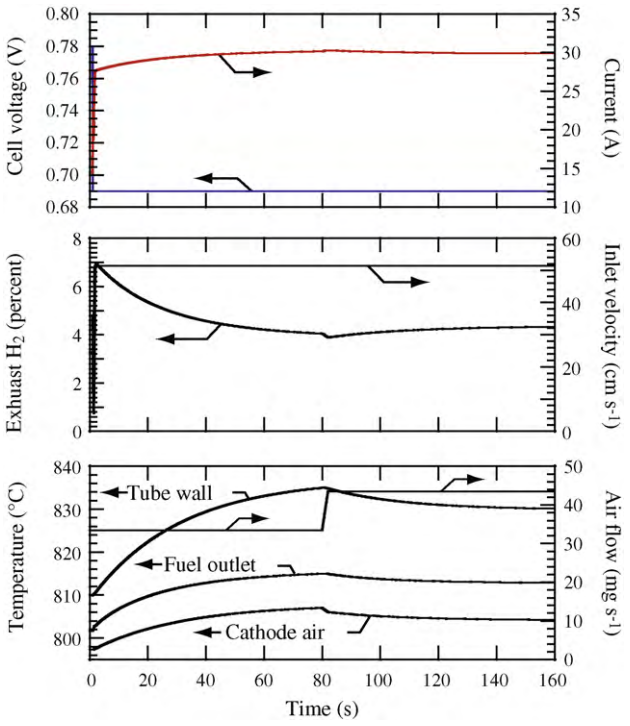

Fig. 9. Total current, exhaust H_2 mole fraction, and temperatures with respect to time in going from a low power demand to a high power demand. The plots capture tube condition changes due to thermal dynamics which are on the order of hundreds of seconds. The results shown for the first 10 s of simulation are exactly the same as those illustrated in Fig. 8. The voltage is dropped from 0.78 V to 0.69 V one second after the start of simulation. The velocity of the fuel inlet is increased from 24.7 cm s^{-1} to 51.4 cm s^{-1} over half a second starting at time equal to 1.2 s. Over the course of half a second, the air flow is raised from 33.5 mg s^{-1} to 43.5 mg s^{-1} starting 80 s into the simulation.

linear, it is possible to extract low-order locally linear models that capture the dominant dynamics of the high-order physical model at particular OPs. The companion paper [1] extends the method to nonlinear system identification over a range of OPs.

Model reduction is accomplished using a data-based approach that is based on the subspace class of system identification methods. In this approach, the physical model takes the role of an experiment, albeit one without measurement noise. This approach, which is an alternative to the direct mathematical linearization of the physical model, has several advantages. First, there is no need to for the physical model to be represented as ordinary differential equation (ODEs) in standard form [i.e., $y' = f(t, y)$]. The physical model used here is expressed as DAEs, not ODEs. Second, a data-based model provides the best linear approximation of the nonlinear system as measured over the amplitude and frequency range of the experimental input, whereas a linearized model has no corresponding approximation qualities.

The linear identification of the (SOFC) stack proceeds as follows. First, a nominal OP for the stack is selected, $(\bar{u}, \bar{y})$, where $\bar{u}$ are the nominal inputs and $\bar{y}$ are the nominal outputs of the stack. A small-signal sequence δu is designed with frequency content that matches the expected system bandwidth. One input is perturbed around its OP, while fixing other inputs at their nominal values. The small-signal response $\delta y = y - \bar{y}$ is recorded. This procedure is repeated for all system inputs. From this data, a single-input single-output (SISO) reduced-order model of each input–output pair is identified. These SISO models are combined into a single multiple-input multiple-output (MIMO) system, and reduced using balanced model-reduction methods [15], resulting in a single (MIMO) reduced-order linear model at a particular OP. As explained briefly in the following section, the subspace system identification is used to capture the small-signal model at a particular OP.

5.1. Subspace system identification

The approach to fit a low-order model to data (here, output from the physical model) is based upon subspace-identification methods. Although this process is well known and documented (e.g., [16]), it is mathematically complex. Only a brief summary is provided here.

An input–output time sequence $(\delta u_k, \delta y_k)$, $(k = 1, \ldots, N)$ obtained and recorded by exercising the physical model at a sampling rate T_s. The objective is to find a linear time-invariant (LTI) system in state-space form,

$$\begin{cases} x_{k+1} = \Phi x_k + \Gamma \delta u_k \\ \delta y_k = C x_k + D \delta u_k \end{cases}, \tag{43}$$

that can closely reproduce the data. The state-space vector is $x_k \in R^n$ and all other vectors/matrices are assumed to have compatible dimensions. The LTI model (Eq. (43)) expresses the relationships among x_{k+1}, x_k, u_k, and y_k over a single sampling interval. The subspace identification proceeds by collecting together larger sampling intervals (windows) of the input–output data. The window length s is a free parameter that should be chosen to be larger than the expected order of the identified system, n. Considering an s-length segment of data, Eq. (43) can be rewritten as

$$\begin{bmatrix} \delta y_k \\ \delta y_{k+1} \\ \vdots \\ \delta y_{k+s} \end{bmatrix} = \begin{bmatrix} C \\ C\Phi \\ \vdots \\ C\Phi^s \end{bmatrix} x_k + \begin{bmatrix} D & 0 & \cdots & 0 \\ C\Gamma & D & \ddots & \vdots \\ \vdots & & \ddots & 0 \\ C\Phi^{s-1}\Gamma & \cdots & C\Gamma & D \end{bmatrix} \begin{bmatrix} \delta u_k \\ \delta u_{k+1} \\ \vdots \\ \delta u_{k+s} \end{bmatrix}. \tag{44}$$

Because the model to be identified is time-invariant (i.e., the Φ, Γ, C, and D matrices are time-independent), any shifted window of the data can be expressed as Eq. (44). The shifted-window input–output data can be expressed in matrix form as

$$Y_s = \Gamma_s X + H_s U_s, \tag{45}$$

where

$$Y_s = \begin{bmatrix} \delta y_k & \delta y_{k+1} & \cdots & \delta y_{k+N} \\ \delta y_{k+1} & \delta y_{k+2} & \cdots & \delta y_{k+1+N} \\ \vdots & \vdots & \vdots & \vdots \\ \delta y_{k+s} & \delta y_{k+s+1} & \cdots & \delta y_{k+s+N} \end{bmatrix}, \tag{46}$$

$$U_s = \begin{bmatrix} \delta u_k & \delta u_{k+1} & \cdots & \delta u_{k+N} \\ \delta u_{k+1} & \delta u_{k+2} & \cdots & \delta u_{k+1+N} \\ \vdots & \vdots & \vdots & \vdots \\ \delta u_{k+s} & \delta u_{k+s+1} & \cdots & \delta u_{k+s+N} \end{bmatrix}, \tag{47}$$

$$X = \begin{bmatrix} x_k & x_{k+1} & \cdots & x_{k+N} \end{bmatrix}, \tag{48}$$

and

$$H_s = \begin{bmatrix} D & 0 & \cdots & 0 \\ C\Gamma & D & \ddots & \vdots \\ \vdots & & \ddots & 0 \\ C\Phi^{s-1}\Gamma & \cdots & C\Gamma & D \end{bmatrix}, \quad \Gamma_s = \begin{bmatrix} C \\ C\Phi \\ \vdots \\ C\Phi^s \end{bmatrix}. \tag{49}$$

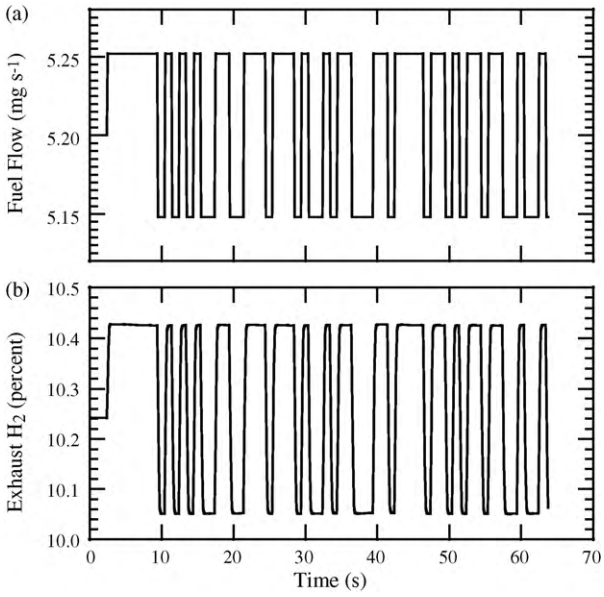

Fig. 10. Small-signal perturbation with fuel flow rate changing with sampling time of $T_s = 0.125$ (s).

The matrix Γ_s is called the extended observability matrix where $s > n$ guaranties Γ_s be full column rank (observability condition). Particular system parameters are contained in H_s and Γ_s, and can be extracted when these terms are known. Following the subspace system-identification approach, estimates of Φ, Γ, C, and D matrices can be evaluated [17]. These steps are briefly explained here. The matrices Y_s and U_s (Eq. (45)) are known from the "measurements" obtained by exercising the physical model with small-signal inputs δu and recording the outputs δy. The $H_s U_s$ term can be removed by multiplying Eq. (45) from right by

$$\Pi_{U_s^T}{}^{\perp} = I - U_s^T (U_s U_s^T)^{-1} U_s, \tag{50}$$

where $\Pi_{U_s^T}{}^{\perp}$ is the orthogonal complement of U_s. As a result, Eq. (45) becomes

$$Y_s \Pi_{U_s^T}{}^{\perp} = \Gamma_s X \Pi_{U_s^T}{}^{\perp}. \tag{51}$$

The singular value decomposition (SVD) of $Y_s \Pi_{U_s^T}{}^{\perp}$ can be represented as

$$Y_s \Pi_{U_s^T}{}^{\perp} = S \Sigma V^T, \tag{52}$$

where S and V are orthonormal matrices and Σ is a diagonal matrix containing the singular values. These matrices can be further partitioned in two parts as

$$S \Sigma V^T = [S_1 S_2] \begin{bmatrix} \Sigma_1 & 0 \\ 0 & \Sigma_2 \end{bmatrix} [V_1 V_2]^T, \tag{53}$$

where Σ_1 contains the first n dominant singular values. Under appropriate condition (i.e., persistently exciting input), the range space of S_1 is the same as Γ_s. Thus, an estimate for Γ_s is taken to be the n first columns of S (Γ_s is defined only within a coordinate transformation of x_k). With Γ_s known, the matrix C (Eq. (43)) is the first p rows of Γ_s, where p is the number of system outputs. The matrix Φ can be determined through the shift pattern of Γ_s. With Φ and C in hand, Γ and D, which are linear in Eq. (45), can be found via solving a linear least squares problem.

5.2. Illustration of linear system identification

This section illustrates the results of linear identification for the (SOFC) stack at a particular OP. The (SOFC) stack variables are partitioned into three inputs and four outputs. The input variables are cell voltage, fuel mass flow rate, and air mass flow rate. The output variables are cell current, hydrogen concentration in exhaust, average MEA temperature, and cathode-exhaust air temperature. As described earlier, the physical model represents a widely disparate range of characteristic time scales. Electrical response is essentially instantaneous (i.e., because electrochemical double-layer charging is neglected, a change in operating voltage causes an instantaneous change in current). Characteristic response time for fluid flow and diffusion is of the order of one second or less. The characteristic times for thermal response is much longer, on the order of minutes. For the purposes of illustrating the system identification, air flow rate and cell temperatures are considered constant. Thus, the illustration here focuses upon identifying cell current and hydrogen concentration from cell voltage and fuel flow rate. In the companion paper [1], a system is identified for the full range of times scales and an MPC controller is designed.

Assume a nominal OP for a stack that is operating at a voltage of $E_{cell} = 0.74$ V, fuel mass flow rate of 5.2 mg s^{-1}, and air mass flow rate of 33.5 mg s^{-1}. Under these conditions, the physical model

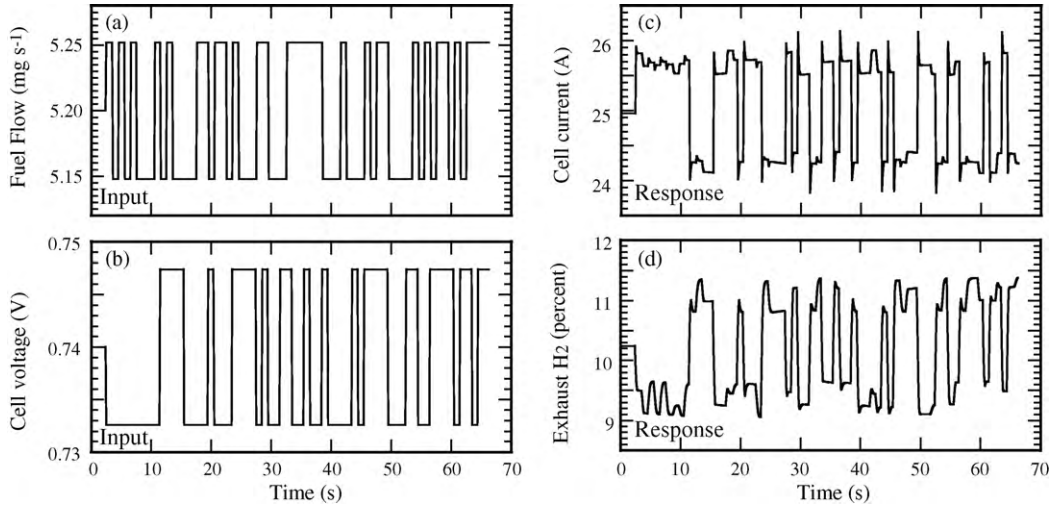

Fig. 11. Comparison between low-order and high-order models for validation simulation.

(single tube) predicts a net current of 24.96 A with 10.24% H_2 mole fraction in fuel outlet. The stack is excited by a perturbation sequence that is suitable for process model identification. In this example, a pseudo random binary sequence (PRBS) with zero mean value is used as the perturbation sequence [18,19]. A sequence of 500 samples is used, with each input perturbed separately. Fig. 10 shows a segment of a simulation at the selected OP. In this perturbation, the fuel flow rate is perturbed with a sampling time of $T_s = 0.125$ s, while the other inputs are held constant at their nominal operating values. Fig. 10a shows the PRBS that is applied as the fuel flow variation. Fig. 10b shows the corresponding change in the H_2 mole fraction in fuel exhaust. The subspace identification at this OP results in a 12th-order small-signal model.

To validate the small-signal model, an input sequence is designed in which all the inputs vary simultaneously. The identified small-signal model should be able to predict the output of this simulation. Fig. 11a and b shows the input variations. Fig. 11c shows the predicted cell current, comparing the high-order physical model and the identified low-order linear model. In this example, the two curves are nearly indistinguishable. Fig. 11d shows another validation result comparing the hydrogen mole fraction in the anode exhaust. Again, the comparison is excellent.

6. Conclusion

A physically based, transient model for a tubular anode-supported (SOFC) is developed as the basis for implementing an MPC controller. Considering the coupled interactions of fuel flow, porous-media transport, heat transfer, reforming chemistry, and electrochemistry, the model is implemented with error-controlled DAE software that enables the accurate prediction of accurate transient responses. Accounting for widely disparate time scales, the model resolves spatial and temporal profiles of composition, temperature, current density, and velocity throughout the cell. Even with approximations to reduce the complexity of the physical model, it is still to large to be incorporated directly into an MPC implementation. Thus, linear model reduction is used to reduce the high-order physical model to a low-order, locally linear model. An example is used to illustrate the validity of the reduced model at a particular OP. As discussed in a companion paper [1], the reduced-order models form the basis for implementing an MPC controller.

References

[1] B.M. Sanandaji, T.L. Vincent, A.M. Colclasure, R.J. Kee, J. Power Sources, submitted for publication.
[2] H. Zhu, R.J. Kee, V.M. Janardhanan, O. Deutschmann, D.G. Goodwin, J. Electrochem. Soc. 152 (2005) A2427–A2440.
[3] H. Zhu, R.J. Kee, J. Electrochem. Soc. 153 (2006) A1765–A1772.
[4] H. Zhu, R.J. Kee, J. Power Sources 169 (2007) 315–326.
[5] H. Zhu, R.J. Kee, J. Electrochem. Soc. 155 (2008) B715–B729.
[6] D.G. Goodwin, H. Zhu, A.M. Colclasure, R.J. Kee, J. Electrochem. Soc. 156 (2009) B1004–B1021.
[7] R.J. Kee, M.E. Coltrin, P. Glarborg, Chemically Reacting Flow: Theory and Practice, Wiley-Interscience, 2003.
[8] E.S. Hecht, G.K. Gupta, H. Zhu, A.M. Dean, R.J. Kee, L. Maier, O. Deutschmann, Appl. Catal., A 295 (2005) 40–51.
[9] E.A. Mason, A.P. Malinauskas, Gas Transport in Porous Media: The Dusty-Gas Model, American Elsevier, New York, 1893.
[10] U.M. Ascher, L.R. Petzold, Computer Methods for Ordinary Differential Equations and Differential-Algebraic Equations, SIAM, Philadelphia, PA, 1998.
[11] A.C. Hindmarsh, P.N. Brown, K.E. Grant, S.L. Lee, R. Serban, D.E. Shumaker, C.S. Woodward, ACM Transactions on Mathematical Software (TOMS) 31 (3) (2005) 396.
[12] D.G. Goodwin An open-source, extensible software suite for CVD process simulation, in: M. Allendorf, F. Maury, F. Teyssandier, (Eds)., Chemical Vapor Deposition XVI and EUROCVD 14, volume PV 2003–08, pages 155–162. Electrochemical Society, 2003. see also http://code.google.com/p/cantera/.
[13] T. Nishino, H. Iwai, K. Suzuki, J. Fuel Cell Sci. Technol. 3 (2006) 33–44.
[14] T.L. Vincent, B.M. Sanandaji, A.M. Colclasure, H. Zhu, R.J. Kee, ECS Trans. 25 (2009) 1175–1184.
[15] B. Moore, IEEE Transactions on Automatic Control 26 (1) (1981) 17–32.
[16] L. Ljung, System Identification: Theory for the User, 2nd edition, Prentice-Hall, 1999.
[17] B.M. Sanandaji, T.L. Vincent, A.M. Colclasure, R.J. Kee, In Proceedings of ASME Dynamic Systems and Control Conference, 2009.
[18] T. Soderstrom, P. Stoica, System Identification, Prentice-Hall, 1988.
[19] Y. Zhu, Multivariable System Identification for Process Control, Elsevier Science, 2001.